Engineering Structures 180 (2019) 685–699

Contents lists available at ScienceDirect

Engineering Structures

journal homepage: www.elsevier.com/locate/engstruct

Parameter identification of wind-induced buffeting loads and onset criteria for dry-cable galloping of yawed/inclined cables

Mohammad Jafari, Partha P. Sarkar*

Aerospace Engineering Department, Iowa State University, 537 Bissell Road, 1200 Howe Hall, Ames, IA 50011, USA

ARTICLE INFO

Keywords:
Dry-cable galloping
Yawed cylinder
Wind-induced cable vibration
Section model tests
Flutter derivatives
Indicial functions

ABSTRACT

Cables of suspension, cable-stayed and tied-arch bridges, suspended roofs, and power transmission lines are prone to moderate to large-amplitude vibrations in wind because of their low inherent damping. Structural or fatigue failure of a cable, due to these vibrations, pose a significant threat to the safety and serviceability of these structures. Over the past few decades, many studies have investigated the mechanisms that cause different types of flow-induced vibrations in cables such as rain-wind induced vibration (RWIV), vortex-induced vibration (VIV), iced cable galloping, wake galloping, and dry-cable galloping that have resulted in an improved understanding of the cause of these vibrations. In this study, the parameters governing the turbulence-induced (buffeting) and motion-induced wind loads (self-excited) for inclined and yawed dry cables have been identified. These parameters facilitate the prediction of their response in turbulent wind and estimate the incipient condition for onset of dry-cable galloping. Wind tunnel experiments were performed to measure the parameters governing the aerodynamic and aeroelastic forces on a yawed dry cable. This study mainly focuses on the prediction of critical reduced velocity (RV_{cr}) as a function of equivalent yaw angle (β^*) and Scruton number (Sc) through measurement of aerodynamic-damping and stiffness. Wind tunnel tests using a section model of a smooth cable were performed under uniform and smooth/gusty flow conditions in the AABL Wind and Gust Tunnel located at Iowa State University. Static model tests for equivalent yaw angles of 0–45° indicate that the mean drag coefficient (C_D) and Strouhal number (St) of a yawed cable decreases with the yaw angle, while the mean lift coefficient (C_L) remains zero in the subcritical Reynolds number (Re) regime. Dynamic one degree-of-freedom model tests in across-wind and along-wind directions resulted in the identification of buffeting indicial derivative functions and flutter derivatives of a yawed cable for a range of equivalent yaw angles. Empirical equations for mean drag coefficient, Strouhal number, buffeting indicial derivative functions and critical reduced velocity for dry-cable galloping are proposed for yawed cables. The results indicate a critical equivalent yaw angle of 45° for dry-cable galloping. A simplified design procedure is introduced to estimate the minimum damping required to arrest dry-cable galloping from occurring below the design wind speed of the cable structure. Furthermore, the results from this study can be applied to predict the wind load and response of a dry cable at a specified wind speed for a given yaw angle.

1. Introduction

Cables of suspension, cable-stayed and tied-arch bridges, suspended roofs and power transmission lines can experience moderate to large-amplitude motions in windy conditions because of their low inherent damping. Structural or fatigue failure of a cable, as a result of these motions, are significant threats to the safety and serviceability of these structures. There are several different types of wind-induced cable vibration such as rain-wind-induced vibration (RWIV) [1–3], vortex-induced vibration (VIV) [4–6], iced-cable galloping [7–9], wake galloping [10,11], and dry-cable galloping [12–16]. Although there have been many experimental and numerical studies related to conventional wind-induced cable vibration, the conditions for onset of dry-cable galloping have not been consistently determined for inclined/yawed cables. In fact, the biggest challenge for cables is to determine the additional damping required to suppress large-amplitude vibrations within their design wind speed. Past studies have shown that dry-cable galloping primarily occurs due to mitigation of Karman vortex shedding generated from axial flow behind yawed cables. Matsumoto et al. [17] showed that dry-cable galloping can occur when there is an artificial axial flow behind the cable. In general, the phenomenon of galloping can be divided into two types: divergent-type galloping (conventional

* Corresponding author.
E-mail address: ppsarkar@iastate.edu (P.P. Sarkar).

https://doi.org/10.1016/j.engstruct.2018.11.049
Received 26 July 2018; Received in revised form 6 November 2018; Accepted 20 November 2018

or classical galloping) and unsteady galloping. The first type, explained using quasi-steady theory, is mainly due to suppression of Karman vortices under stationary conditions, and the second type occurs when Karman vortices are not fully mitigated by axial flow and exhibit some amount of unsteady response with non-stationary amplitude. To specify the onset of divergent response to dry-cable galloping, the proposed empirical criterion based on wind tunnel experiments is the critical reduced velocity, $RV_{cr} = cSc^p$, where c and p are constants, and $Sc = m\zeta/\rho D^2$ is the Scruton number. Honda et al. [18] specified $c = 54$ and $p = 2/3$, and Irwin [19] defined the constants as $c = 35$ and $p = 1/2$. Another way to determine the critical reduced velocity is based on aerodynamic damping expressed in terms of flutter derivatives of a cable section, particularly H_1^* that determines the aerodynamic damping in a vertical plane of vibration. It can be shown that dry-cable galloping occurs when aerodynamic damping ζ_{aero} becomes negative enough to offset the mechanical damping when $H_1^* = -\frac{4\zeta_{aero}}{\rho D^2} = 4Sc$ [17]. Although other instability criteria have been introduced, e.g. FHWA (Federal Highway Administration of U.S.) [20] and Saito [21], who previously proposed formulae or instability boundaries, there has no specification of the criteria corresponding to the yaw and/or inclination angle of a cable. In this paper, a criterion for dry-cable vibration is presented through the prediction of critical reduced velocity (RV_{cr}) as a function of yaw angle (β) and Scruton number (Sc) of cables based on wind-tunnel measurements of their aerodynamic damping and aerodynamic stiffness.

Aerodynamics of cables have been widely investigated using both experimental and numerical techniques because significant damage in cables has been reported in suspension/cable-stayed bridges. Cheng et al. [22,23] experimentally investigated the effects of some parameters, including Reynolds number, surface roughness, and wind speed on yawed/inclined dry-cable galloping. They indicated that the most divergent motions occurred when Scruton number and wind speed were 0.88 and 32 m/s, respectively. Duy et al. [24] studied dry-cable galloping by conducting experimental tests, and they illustrated the effects of spiral wire on smooth cable surfaces. Dynamic experiments showed that divergent galloping occurs only for yawed angles of 30–60°. Matsumoto et al. [25] described the underlying mechanisms of dry-cable galloping for wind-induced vibration through a series of experimental tests that employed splitter plates with various perforation (or porosity) ratios placed behind the cable in its wake to control the Karman vortices. These results illustrated that the intensity of a Karman vortex decreases and divergent galloping arises when the perforation ratio decreases. Katsuchi and Yamada [26] carried out wind tunnel experiments to investigate galloping phenomenon of dry-cables along the vertical direction. They showed that dry galloping occurred for both indented and smooth surfaces. Benidir et al. [27] conducted a series of experimental tests to determine influence of roughness and circularity defects on instability of dry-cable galloping, with Reynolds number in the subcritical region to study the establishment of bubble on one side of a cylinder. Flamand and Boujard [28] measured the pressure distribution around cables at different yawed angles and concluded that one solution for mitigating the vibration is to increase the surface roughness. Hence, using helical wires on cables is not only beneficial with respect to rain-wind induced vibration, but also helpful with respect to dry-cable galloping. Kleissl and Georgakis [29] studied the effect of helical fillets and pattern-indented surfaces on the aerodynamics of yawed cable. They employed oil visualization tests to demonstrate the difference between the aerodynamics of yawed cable with helical fillets and those with pattern-indented surfaces. Ma et al. [30] investigated the effect of Reynolds number on dry galloping by modeling cylinders with semi-elliptical cross-sections. They determined that a semi-elliptical cross section causes instability of aerodynamic forces, and this explains why dry-cable galloping occurs in yawed/inclined cables. Nikitas and Macdonald [31] studied the aerodynamic characteristics of dry-cable galloping by performing wind tunnel experiments. They found unsteady behavior in the critical Reynolds number range, and indicated that inclination angles were the most important parameters affecting this phenomenon.

Macdonald and Larose [32] derived a theoretical formulation of dry-cable galloping using quasi-steady theory to simplify the equations and derive formulae for such a three-dimensional phenomenon. They provided an equation to calculate aerodynamic damping that was very useful for determining stability or instability of a yawed/inclined cable under dry conditions. Raeesi et al. [33] studied theoretically dry-cable galloping, and they revealed the effect of unstable/turbulent flow on computing the aerodynamic damping ratio. They applied their method to evaluate the aerodynamic stability of stay-cables in a cable-stayed bridge in unsteady wind, where their results satisfactorily predicted aerodynamic instability. Wu et al. [34] used computational fluid dynamics (CFD) methods in a high accuracy model to simulate fluid flow over a yawed cable. Delayed detached eddy simulation (DDES) yielded numerical results and experimental data that were in a good agreement. Yeo and Jones [35] studied the effect of yawed angle on dry-cable galloping using numerical simulation. They carried out their modeling for different angles from 0° to 60°, applied a DES model for simulation, and concluded that the strength of Karman vortices diminishes at increasing yaw angles.

This paper focuses on dry-cable galloping by conducting static and dynamic wind tunnel experiments on section models of smooth cylinders representing a section of cables under uniform and smooth flow conditions. The twist or torsional motion of the cable that would be important to consider for cables with non-circular cross section as in iced cables [36] is neglected here in the dynamic analysis of smooth cables. Static data led to proposing empirical equations for drag coefficient and Strouhal number as functions of yaw angle. To define self-excited and buffeting loads, flutter derivatives and buffeting indicial derivative functions were extracted for different yaw angles using a free vibration system and a gust generator, respectively. All experiments were carried out in one-degree-of-freedom vertical motion (h) of a section model of a cable at yaw angles ranging from 0° to 45°; since real cables experience vibration due to dry-cable galloping along an inclined plane with a significant vertical component that plays a critical role in their instability. The maximum yaw angle of 45° for the tests was chosen because it was determined to be the critical yaw angle for dry-cable galloping of horizontal cables [17]. Since finding the required damping to prevent dry-cable galloping has been a challenge for many years, a practical design procedure is introduced based on the experimental results to estimate the required damping at a given design wind speed. Moreover, these results can be applied to simulate the vibration of a dry smooth cable in turbulent wind with mean wind speeds outside the lock-in range of vortex-induced vibration, where the mean wind speed and mean wind direction change with height in the atmospheric boundary layer (ABL).

2. Methodology

2.1. Equations of motion

In general, wind loads that act on a structure can be classified as static and dynamic for the purpose of analysis. Dynamic loads are important because they can cause structural fatigue or failure over long or short periods. The dynamic loads are defined either in frequency- or time-domain. While equations of motion of a structure under wind loads can be written for all three degrees of freedom of the structure, two lateral and one torsional directions, only along-wind and across-wind motions are considered important for a cable because torsional motion is negligible compared to others. External wind loads on a cable cross-section can be divided into vortex shedding, buffeting, and self-excited loads. Fig. 1 shows dynamic wind loads and velocity components for a circular section of a cable. The equations of motion for across-wind or vertical (h) and along-wind or lateral (p) motions can be

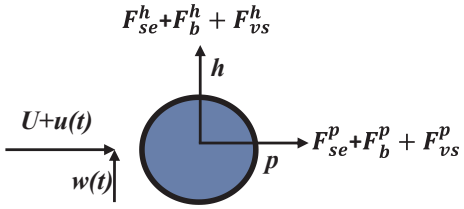

Fig. 1. Schematic view of dynamic wind loads and velocity components over a smooth cable.

written as follows:

$$m(\ddot{h} + 2\omega_h\zeta_h\dot{h} + \omega_h^2 h) = F_{se}^h + F_b^h + F_{vs}^h \quad (1)$$

$$m(\ddot{p} + 2\omega_p\zeta_p\dot{p} + \omega_p^2 p) = F_{se}^p + F_b^p + F_{vs}^p \quad (2)$$

where m is mass per unit length, h and p are vertical and lateral displacements, ω_h and ω_p are natural frequencies, ζ_h and ζ_p are total damping ratios, and F_{se}, F_b, and F_{vs} are self-excited, buffeting, and vortex shedding-induced loads per unit length of a cable; U is mean wind speed while $u(t)$ and $w(t)$ are along-wind and across-wind turbulence components, normal to the cable axis. Different system identification methods can be applied to extract the parameters of each of the above wind load components using a section model of a yawed cable that can then be employed to calculate the dynamic wind loads for the real cable. Since vortex-induced vibration (VIV) of cables produce low amplitude motions compared to other types of wind excitation and occurs over a narrow range of wind speeds, self-excited and buffeting loads are only considered in this study, as briefly described in the following sections.

In this study, a free vibration test was used to identify the flutter derivatives (FD) of a cable. Flutter derivatives have been widely used to find the flutter wind speed of different structures, mainly long-span bridges, and many studies have been conducted to extract flutter derivatives using section models. Flutter derivatives associated with vertical and lateral motions are listed in Table 1. More descriptions about self-exited and buffeting loads are presented in Appendices A and B.

3. Experimental setup

According to the literature, dry-cable galloping occurs mostly in inclined cables above a critical wind speed within a certain range of yaw angles. The past few studies [17,25] have indicated that the aerodynamic behavior of a non-inclined ($\alpha = 0^\circ$) cable is equivalent to an inclined cable based on the definition of an equivalent yaw angle (β^*). The concept of using equivalent yaw angle was verified by other researchers [14,26,37] to show its reliability in extraction of aerodynamic properties of an inclined cable for dry-cable galloping and rain-induced vibration. Therefore, the concept of equivalent yaw angle was used in this study to extract the aerodynamic properties a yawed and/or inclined section model for prediction of load and response. Hence, the present study was carried out on a non-inclined section model to determine the aerodynamics of a yawed/inclined cable. In this study, a horizontal rigid section model with a finite length that represents a section of a cable has been used to predict the critical reduced velocity for dry-cable galloping at a given Scruton number of the cable model. However, a numerical/analytical approach that uses the aerodynamic properties of a yawed cable as presented here can be used to simulate the cable response and predict the critical velocity for dry galloping of an inclined cable or a horizontally suspended cable more accurately by considering sag due to cable weight, boundary conditions at both ends of the cable, yaw angle, inclination angle, and variation of wind speed with elevation in atmospheric boundary layer. The definitions of inclination angle (α), actual yaw angle (β), and equivalent yaw angle (β^*) are shown in Fig. 2a and b. Eq. (3) relates actual yaw angle and inclination angle to the equivalent yaw angle. Since all experiments in this study were conducted for a non-inclined cable ($\alpha = 0$), actual yaw angle and equivalent yaw angle are equal ($\beta = \beta^*$), and yaw angle in this study refers to equivalent yaw angle in all the results presented here.

$$\beta^* = \sin^{-1}(\sin\beta\cos\alpha) \quad (3)$$

Table 1
Flutter derivatives (FDs) associated with vertical and lateral motions of a cable.

	Degree of freedom (DOF)	FDs
1	1DOF vertical (h)	H_1^*, H_4^*
2	1DOF lateral (p)	P_1^*, P_4^*
3	2DOF (h, p)	H_1^*, H_4^*, H_5^*, H_6^* P_1^*, P_4^*, P_5^*, P_6^*

All wind tunnel tests in this paper were carried out in the aerodynamic test section of the Aerodynamic and Atmospheric Boundary Layer (AABL) Wind and Gust tunnel located in the Wind Simulation and Testing Laboratory (WiST Lab) of the Department of Aerospace Engineering at Iowa State University. This wind tunnel has two test sections, an aerodynamic test section of 2.44 m (8.0 ft.) width × 1.83 m (6.0 ft.) height with a maximum wind speed capability of 53 m/s (173.9 ft/s), and an ABL test section of 2.44 m (8.0 ft.) width × 2.21 m (7.25 ft.) height with a maximum wind speed (average) capability of 40 m/s (131 ft/s).

3.1. Data acquisition system

The 1DOF dynamic wind tunnel test rig that was used here includes two elastic spring systems, one at each end of the section model, consisting of an air bearing connected to four springs that freely slides over a polished rod and a uniaxial load cell fixed at the end of one spring (Fig. 3a). The load cell measures the elastic force in the spring that is converted to displacement using the spring stiffness. For dynamic force measurements, the sampling frequency and sampling time were 1000 Hz and 60 s, respectively. LabVIEW software was used for data acquisition from two load cells, one on each side of the section model, one connected on the top and the other on the bottom. The resultant model displacement for each of the three data runs of 60 s is computed from the average of the force data from the two load cells. The placement of diagonally opposite load cells helped to cancel out any spurious modes of vibration about the horizontal axis along the wind direction. The average values of the identified load parameters from the three data runs are computed and presented here. Aerodynamic loads for the static tests were measured by two six-component force balances (JR3), fixed at each end of the section model (Fig. 3b). The JR3 has a precision of ± 0.25% of its maximum load capacity of 40 N. Both JR3s were fixed to the two ends of the model axis to record the forces in X, Y, and Z directions.

For static force measurements, the sampling frequency was 500 Hz, and the sampling time was 60 s. For pressure measurement, two 64-channel pressure modules (Scanivalve ZOC 33/64 Px) were utilized to capture the pressure distribution on the cylindrical model with the sampling frequency of 250 Hz and the sampling time of 60 s. A Cobra probe (4-hole velocity probe) was used to record point-wise measurement of the upstream wind velocity with a sampling frequency of 1250 Hz and a sampling time of 60 s.

3.2. Static test setup

A new setup was built to measure the aerodynamic/aeroelastic loads and pressure distributions for the static and dynamic wind tunnel tests of the yawed cable models. As shown in Fig. 4, this setup properly secures the cable model for yaw angles ranging from 0° to 45°. The setup is also capable of testing two models in tandem for wake

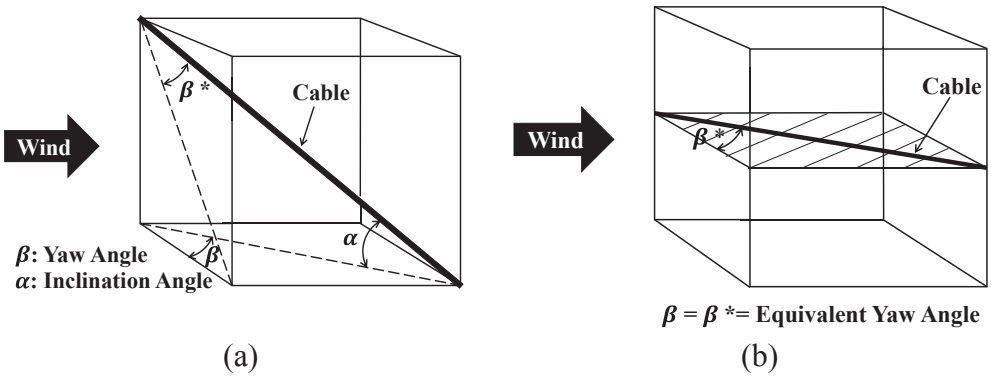

Fig. 2. Definition of actual yaw angle and equivalent yaw angle, (a) yawed/inclined cable, (b) yawed cable.

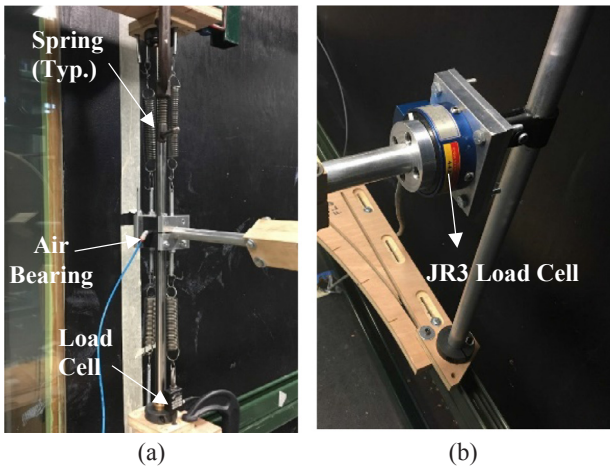

Fig. 3. Test setup for measurements, (a) 1DOF dynamic, and (b) static.

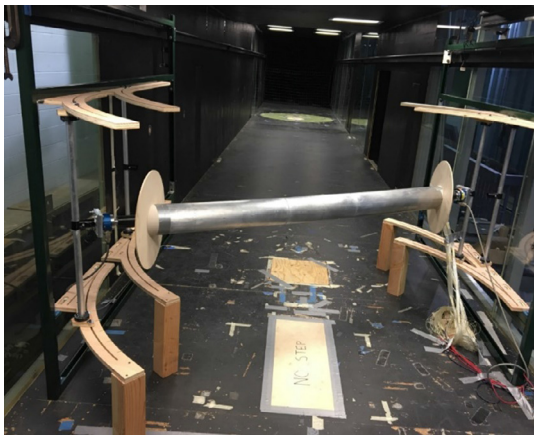

Fig. 4. Static test setup of yawed cable with end plates for pressure and force measurements.

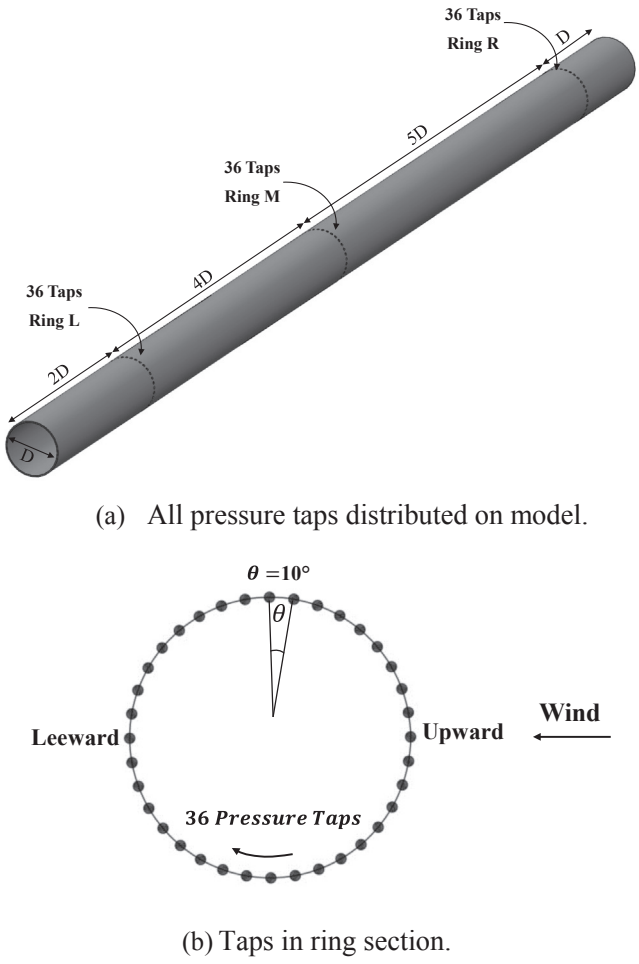

Fig. 5. Pressure tap arrangement on the cable model surface.

galloping. An aluminum polished tube of diameter (D) 127 mm and of length (L) 1.52 m was used to represent a smooth cable. Although the aspect ratio (L/D = 12) was large enough to prevent edge effects, two circular end plates with diameter of 4D were attached to both sides of the cable model, parallel to the upstream airflow, to generate the 2D flow over the cable model. Fig. 4 displays the yawed smooth cable with two end plates in the setup. As shown in Fig. 5a, the cable model had 108 pressure taps distributed on its surface for measuring local pressures. There were 36 pressure taps at equal angular spacing of 10 degrees along each of the three rings located on the cylinder and spaced 4D or 5D distance apart (see Fig. 5a and b). The blockage ratio was less than 5% for all experiments. The cable model was tested in uniform and smooth (< 0.2% turbulence) wind flow with wind speeds ranging from 5.9 to 22.6 m/s.

3.3. Buffeting test setup

For the buffeting experiments, an aluminum polished tube of diameter (D) 127 mm and of length (L) 0.61 m was used as the cable model. Two circular end plates with a diameter of 4D were attached to both sides of the model, parallel to the upstream airflow, to generate the 2D flow over the cable model. The aspect ratio (L/D = 4.8) of the cable model was kept larger than the correlation length ($L/D \approx 4$) of

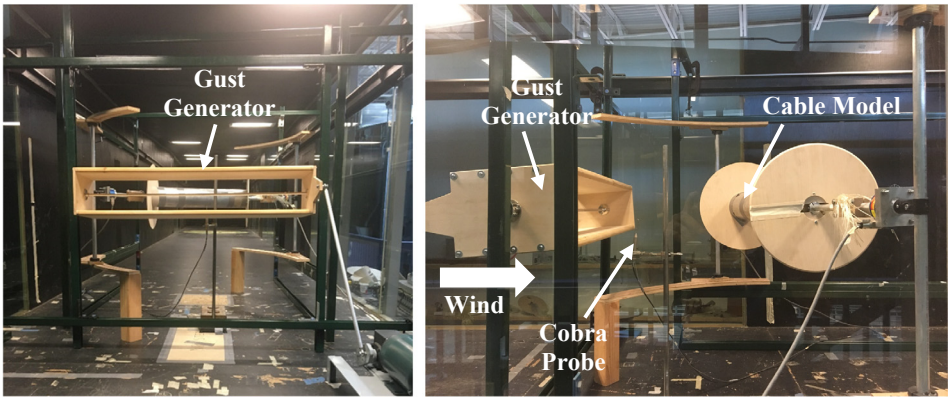

(a) Front view (b) Side view

Fig. 6. Buffeting setup including gust generator system, Cobra probe, and yawed model.

the wind loads along the model length. Fig. 6 shows the cable model with a gust generator that was fixed upstream of the model to generate a sinusoidal gust at a fixed frequency and amplitude that is uniform over the model's length. The wind upstream of the gust generator was uniform and smooth. The gust generator (two thin plates in parallel with a gap) was supported by a frame and connected to a motor by a rod, enabling it to oscillate at a specific frequency and amplitude. A load cell (JR3) was fixed on each side of the cable model for measuring the loads. The upstream wind speed of the cable model was recorded by a velocity probe (Cobra probe, ®Turbulent Flow Instrumentation) located 20 cm downstream of the gust generator. The relative locations of the gust generator, Cobra probe and cable model are shown as side view in Fig. 6b. A LabVIEW program was developed to record the fluctuating aerodynamic loads (lift and drag) on the cable model in the time domain where the data was measured at a sampling frequency of 100 Hz. The power spectral densities (PSDs) of the upstream wind turbulence and aerodynamic loads were calculated to estimate the aerodynamic admittance functions at a fixed reduced frequency (K). The tests were repeated at varying wind speed and different gust frequencies to cover the range of reduced frequency over which the aerodynamic admittance functions were desired. The procedure was repeated for several yaw angles of the cable model, namely, 0°, 15°, 30°, and 45°.

3.4. Dynamic test setup

A new and lighter cable model was used for dynamic tests because a low Scruton number was required to capture galloping. All details of the dynamic test setup and the cable section model are summarized in Table 2 for both 1DOF tests, vertical (h) and lateral motions (p). The dynamic test rig shown in Fig. 7a has the capability to simulate only vertical motion whereas the one in Fig. 7b has the capability to simulate motions in all 3DOF (vertical, lateral and torsional). However, the 3DOF test rig also allows testing of models along any coupled (vertical-lateral, vertical-torsional, etc.) DOFs or single DOF by arresting the motion along one or two DOFs as desired. Here only 1DOF tests for vertical motion (h) or lateral motion (p) are conducted as shown in Fig. 8a and b, respectively. The test rig and data acquisition have been described earlier in Section 3.1. These tests were repeated for several yaw angles of the cable model, namely, 0° and 15° to 45° with increments of 5°, for the vertical case. The tests for the lateral motion was carried out only for a yaw angle of 45° since the results from the vertical motion showed that this yaw angle was the most critical for galloping.

Table 2
Properties of model and setup for dynamic tests.

	Value (1DOF)
Diameter (D)	102 mm
Length (L)	1.52 m
	Vertical
Total stiffness (K_h)	560 (N/m)
Total mass (M_h)	3.6 kg
$m_{eh}(M_h/L)$	2.36 kg/m
Natural frequency (n_h)	1.99 Hz
Damping ratio (ζ_h)	0.0041
Scruton number ($Sc_h = \frac{m_{eh}\zeta_h}{\rho D^2}$)	0.77
	Lateral
Total stiffness (K_p)	560 (N/m)
Total mass (M_p)	6.8 kg
$m_{ep}(M_p/L)$	4.46 kg/m
Natural frequency (n_p)	1.44 Hz
Damping ratio (ζ_p)	0.0035
Scruton number ($Sc_p = \frac{m_{ep}\zeta_p}{\rho D^2}$)	1.24

4. Results and discussion

4.1. Static test

The aerodynamic force coefficients were calculated based on surface pressures on the cable model and validated with those from direct load measurements. Power spectral densities (PSD) of lift coefficient are plotted for the yaw angle $\beta = 0^\circ$ against reduced frequency $K = fD/U$ for a range of Reynolds numbers (Re) in Fig. 8 which shows a single peak at $K = K_s = 0.20$. These results indicate that the Strouhal number ($St = \frac{f_s D}{U} = K_s$, f_s is von-Karman vortex shedding frequency) for $\beta = 0^\circ$ does not change in the subcritical regime of Reynolds number, and in fact it is almost constant ($St(\beta = 0^\circ)$=0.20). Fig. 9 shows the PSD of drag coefficient for $\beta = 0^\circ$ case where two peaks are seen with the second peak frequency twice the first one, confirming past studies. In this study, Strouhal number of yawed cable was measured to identify the "lock-in" wind speed for vortex-induced vibration where buffeting response equations will not apply for a yawed cable. In Fig. 10, the Strouhal number, identified from the PSDs of lift coefficient records, is plotted as a function of yaw angles corresponding to the subcritical Reynolds number regime where it is almost constant. It shows that the Strouhal number decreases as yaw angle increases. An empirical equation (Eq. (4)) was obtained by curve-fitting to predict the Strouhal number at different yaw angles. Additionally, the results of Strouhal number for a yawed cable confirm that the normal Strouhal number is

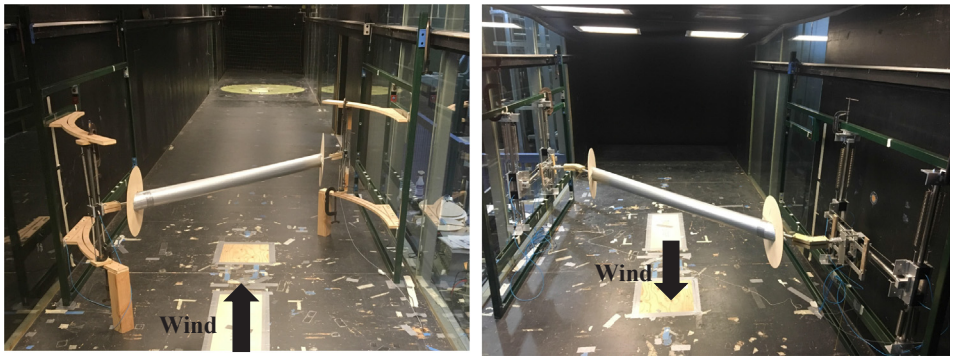

(a) Vertical motion (b) Lateral motion

Fig. 7. Dynamic test setup (1DOF) for extracting self-excited loads (flutter derivatives) of a yawed cable.

constant ($St_n(\beta) = 0.2$) and follows the independence principle [34]. This occurs because the separation point has been proven independent of yaw angle that means crosswise component of the vortex shedding is not influenced by spanwise flow [38].

$$St(\beta) = St(0) \times \cos\beta = 0.2\cos\beta \quad 0° \leqslant \beta \leqslant 45° \tag{4}$$

In Fig. 11, mean drag coefficient ($C_D(\beta) = \frac{\bar{F}_D}{0.5\rho U^2 DL}$) is illustrated for various yaw angles over a range of Reynolds numbers. These results indicate that drag coefficient is reduced when yaw angle is increased. It should be noted that cable stiffness or frequency of vibration is proportional to cable tension that depends on the pre-tension in the cable, cable weight and aerodynamic drag. Thus, as drag diminishes at higher yaw angles, the cable stiffness will reduce making yawed cables vulnerable at higher wind speeds. Since the drag coefficient of a yawed circular cylinder for $0° \leq \beta \leq 30°$ is almost constant in a subcritical Reynolds number (Re) range, the average drag coefficient is depicted in Fig. 12 for this range of yaw angles. In this figure, the highest value of drag coefficient is plotted for $\beta = 45°$ case for the range of Re investigated. An empirical equation (Eq. (5)) has been proposed using curve-fitting to predict the mean drag coefficient as a function of yaw angle while the factor of $F(Re, \beta)$ is applied to consider the effect of yaw angle and Reynolds number for yaw angles larger than 30° due to variation in drag coefficient. It was assumed that the effect of yaw angle from 30° to 45° is linear on drag coefficient. The results show that the drag coefficient decreases with increasing yaw angle that occurs because the cross section of yawed cable changes from circular to elliptical with increasing yaw angle. Since an elliptical cross section is a streamlined body with smaller wake region, it has a smaller drag coefficient compared to a circular section. Additionally, it can be seen that the drag coefficient reduction occurs for yaw angle of 45° at a lower Reynolds number because the elliptical section has a lower critical Reynolds number compared to a circular one, and it depends on the aspect ratio of the ellipse. The mean lift coefficient ($C_L(\beta) = \frac{\bar{F}_h}{0.5\rho U^2 DL}$)was measured to be zero for all the yawed cables tested for $0° \leq \beta \leq 45°$ in the subcritical Reynolds number (Re) range. Past studies have shown that inclined cables with non-circular cross section have non-zero mean lift coefficient and are especially vulnerable to dry galloping near its critical Reynolds number; negative aerodynamic damping is generated as shown by quasi-steady theory. However, it is also shown that yawed cables with smooth surface, which has zero mean lift coefficient in subcritical range of Reynolds number, can experience dry galloping in this range [24].

$$C_D(\beta) = C_D(0) \times (0.8\cos^2\beta + 0.2\cos\beta) \times F = (0.96\cos^2\beta + 0.24\cos\beta) \times F(\mathrm{Re},\beta°) \tag{5}$$

$$F(\mathrm{Re},\beta°) = \begin{cases} 1 & 0° \leqslant \beta \leqslant 30°, \quad 0.5\times10^5 \leqslant \mathrm{Re} \leqslant 2.2\times10^5 \\ 1.379 \times (1.778 \times 10^8 \mathrm{Re}^{-1.746} + 1) \times (-0.0125\beta° + 1) & 30° \leqslant \beta \leqslant 45°, \quad 0.7\times10^5 \leqslant \mathrm{Re} \leqslant 2.7\times10^5 \end{cases}$$

4.2. Buffeting test

The buffeting indicial derivative functions (Eq. (B.5)) are required for calculation of across-wind (lift) and along-wind (drag) buffeting

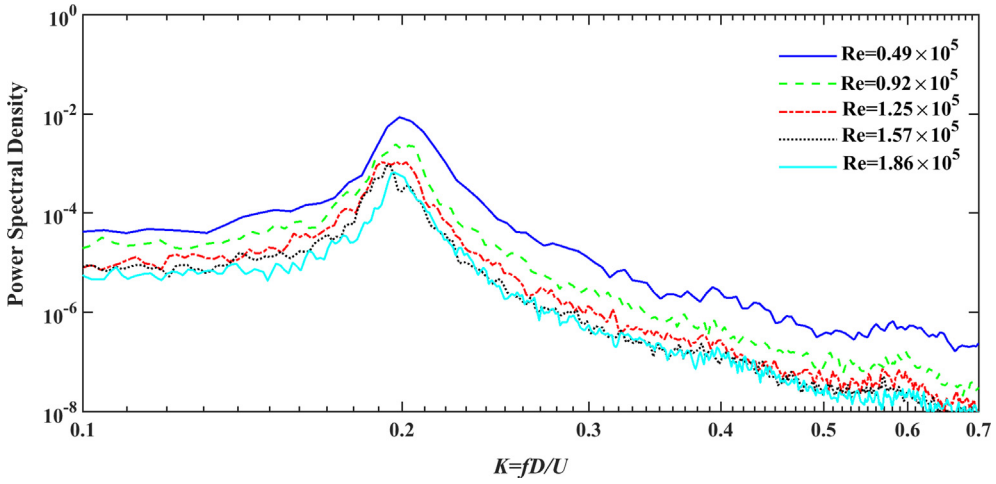

Fig. 8. Power spectral density of lift coefficient for different Reynolds numbers at $\beta = 0°$.

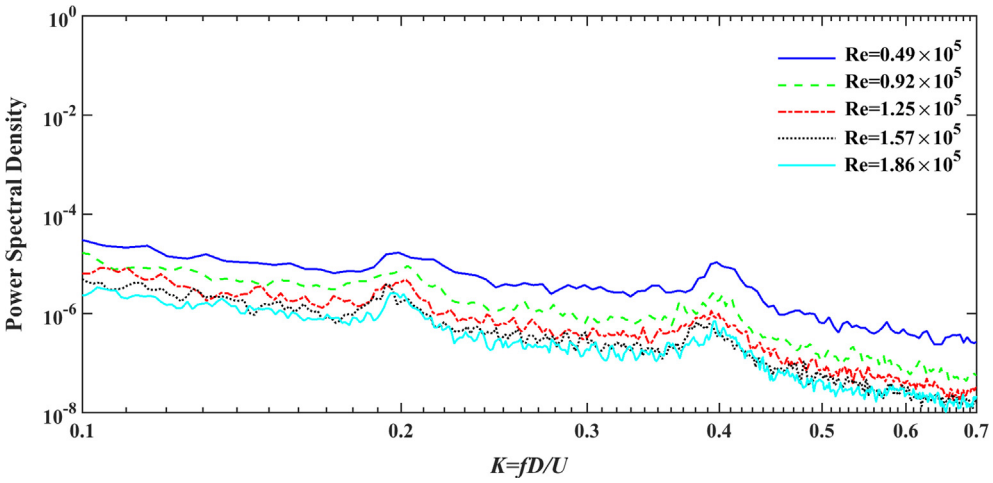

Fig. 9. Power spectral density of drag coefficient for different Reynolds numbers at $\beta = 0^{\circ}$.

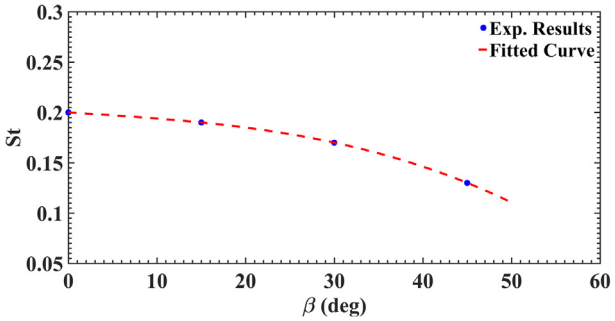

Fig. 10. Strouhal number as a function of yaw angle for smooth cable.

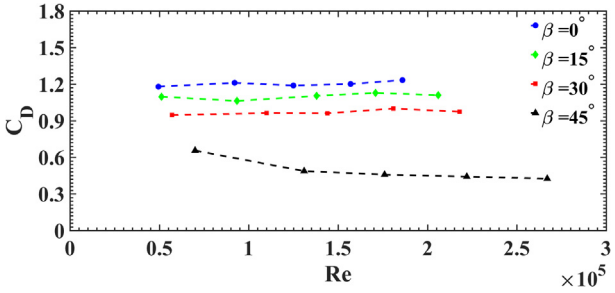

Fig. 11. Drag coefficient vs. Reynolds number of cable for different yaw angles.

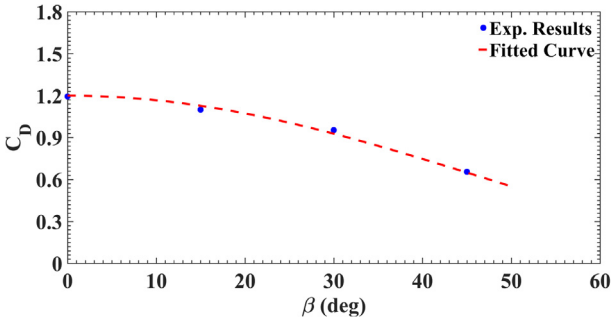

Fig. 12. Drag coefficient as a function of yaw angle for smooth cable.

loads in the time domain. The procedure explained in Section 2 for extracting these functions was used where the aerodynamic admittance functions associated with lift and drag of the cable (Eqs. (B.3)–(B.4)) for yaw angles (β) of 0°, 15°, 30°, and 45° were first identified, and then the constants A_1 to A_4 in Eq. (B.5) were calculated using Eq. (B.6). The frequency of the gust (ω) and mean wind speed (U) were changed to cover a range of reduced frequency ($K = \omega D/U$)varying approximately from 0.2 to 0.7. Since the mean lift coefficient was zero for all yawed cable models in the subcritical Reynolds number regime, the first term in Eq. (B.3) and the second term in Eq. (B.4) are zeroes. Fig. 13 shows that the aerodynamic admittance function in the along-wind direction (χ_p^2) has a lower value at higher yaw angles whereas the aerodynamic admittance function in the across-wind direction (χ_h^2) has a higher value at higher yaw angles. In Fig. 13, buffeting indicial derivative functions ϕ_h' for across-wind direction and ϕ_p' for along-wind direction. The aerodynamic admittance functions are often fitted by a curve with an equation in the form $1/(1 + CK)$, and therefore the constant coefficient (C) for each of the fitted curves is identified and plotted for the across and along-wind directions in Fig. 14 based on equations presented in Fig. 13. Two empirical equations, Eqs. (6) and (7), are proposed for predicting the aerodynamic admittance functions for different yaw angles, so these equations can be used to calculate the derivatives of indicial functions for yaw angles ranging from 0° to 45°.

$$\chi_h^2(K, \beta^{\circ}) = \frac{1}{1 + C_h K},\ C_h = -7.11 \times \beta^{\circ} + 316.9 \quad 0^{\circ} \leqslant \beta \leqslant 45^{\circ} \tag{6}$$

$$\chi_p^2(K, \beta^{\circ}) = \frac{1}{1 + C_p K},\ C_p = 0.061 \times \beta^{\circ} + 12.21 \quad 0^{\circ} \leqslant \beta \leqslant 45^{\circ} \tag{7}$$

4.3. Dynamic test

As described in Section 2, displacement time history of the section model in free vibration was calculated from the recorded load measurements by two load cells attached to the elastic springs, and then a low-pass filter “Butterworth” was used to filter the noise from the original data. Fig. 15 displays a typical time history comparison between the original displacement data and the filtered displacement data. Vertical DOF (h) flutter derivatives (H_1^*, H_4^*)of the cable were extracted for different yaw angles using the ILS method, and plotted with respect to the reduced velocity ($RV = U/nD$) in Fig. 16. The trend of H_1^* shows that it starts increasing (less negative) for the yaw angles greater than zero after a certain reduced velocity. Therefore, positive aerodynamic damping that is proportional to the negative of H_1^* will potentially become negative after a critical reduced velocity. Fig. 16a shows that the flutter derivative H_1^* becomes positive beyond a specific reduced velocity that is influenced by the interaction of axial flow and vortex shedding of a yawed cable. The strength of vortex shedding becomes less as the velocity of axial flow behind the yawed cable increases, and this complex interaction between two flows has a direct effect on variation of aerodynamic damping. Amongst all the yaw angles explored here, $\beta = 45^{\circ}$ was found to have the lowest critical reduced velocity.

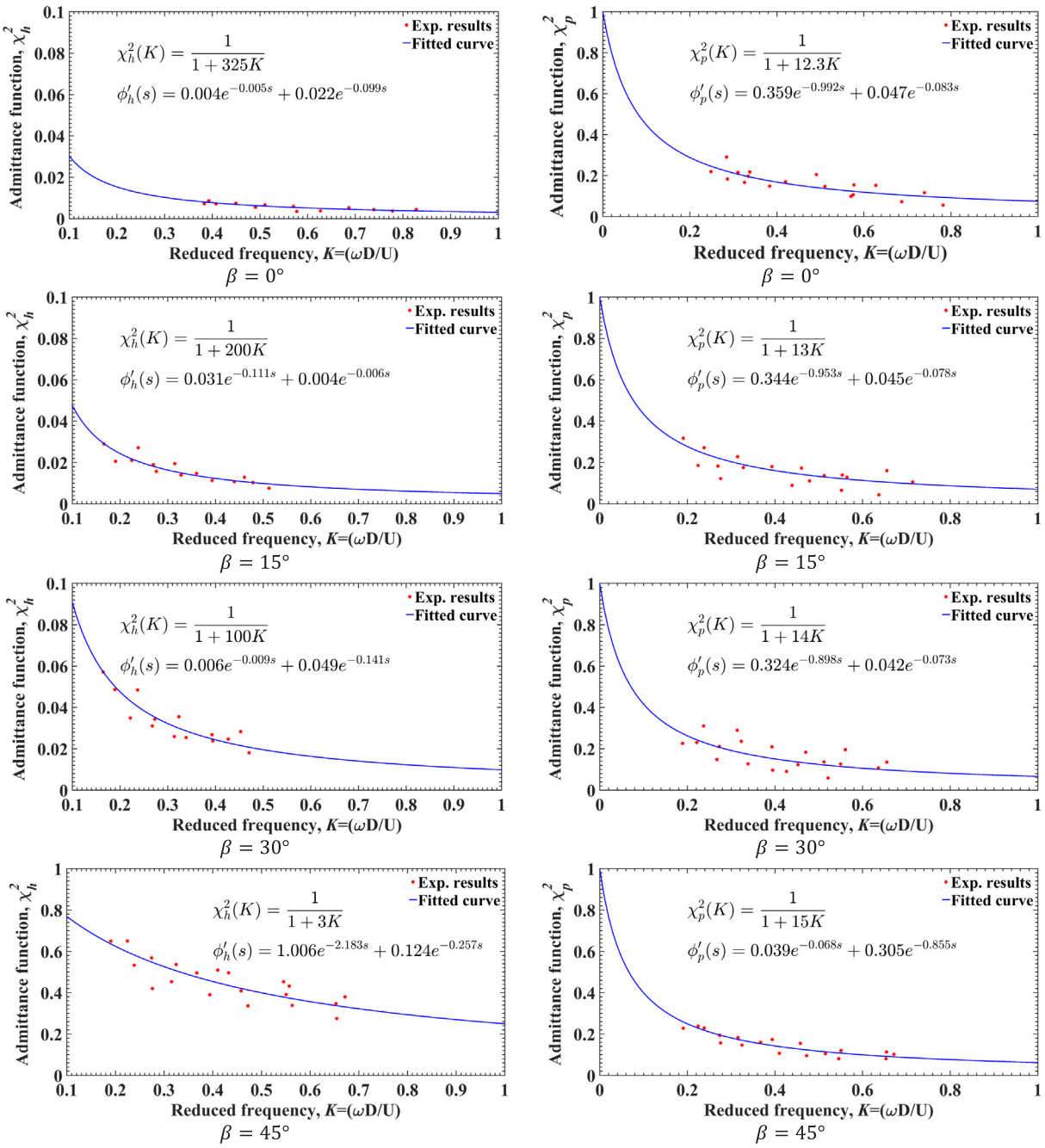

Fig. 13. Aerodynamic admittance and buffeting indicial derivative functions in across-wind (ϕ_h') and along-wind (ϕ_p') directions of a circular cylinder.

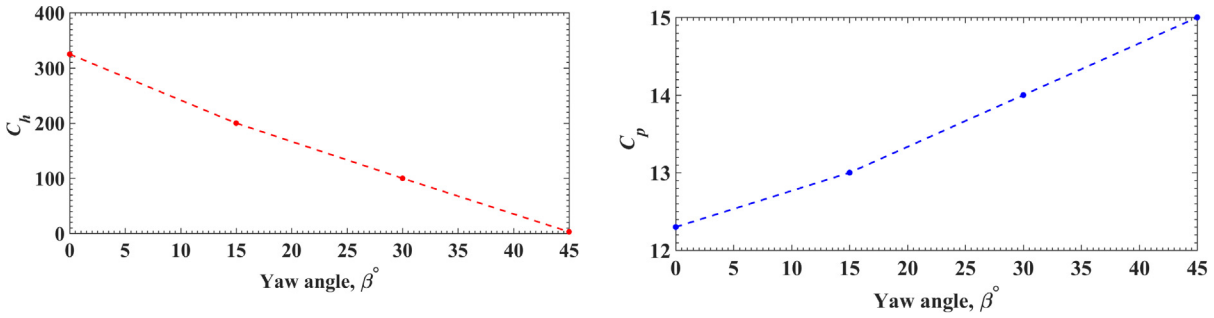

(a) Across-wind (b) Along-wind

Fig. 14. The constant (C) appearing in the generalized form of the aerodynamic admittance function, $1/(1 + CK)$, of a circular cylinder as a function of yaw angle.

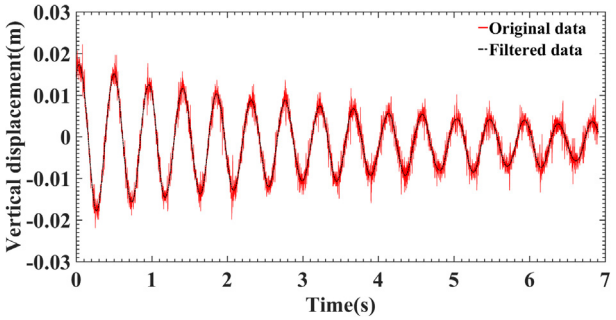

Fig. 15. Displaying the original and filtered displacement.

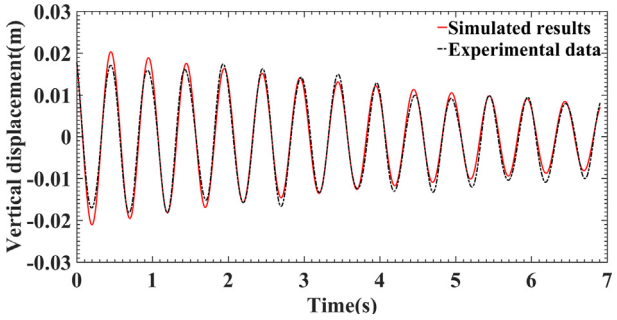

Fig. 17. Comparison of vertical displacement time history for $\beta = 45°$ at velocity of 5.9 m/s.

The wind tunnel tests to extract the flutter derivative H_1^* were limited up to a certain reduced velocity because the cable model started displaying large amplitude motions at higher reduced velocities. To verify the extracted flutter derivatives based on measurements, the time history of the measured displacement and simulated displacement based on the extracted flutter derivatives are compared. One typical comparison is plotted in Fig. 17, showing a good agreement with one another. As explained before, it has been theoretically proven that the critical velocity for divergent motion or galloping of the cable in the vertical direction occurs at $H_1^* = 4Sc$ when the aerodynamic damping offsets the mechanical damping producing zero net damping. The results of H_1^* (Fig. 16a) for different yaw angles were fitted by a curve as a function of reduced velocity ($H_1^* = f(RV)$), after which the equation of $H_1^* = f(RV) = 4Sc$ was solved for a range of Scruton numbers (0.5–6) to determine the critical reduced velocity (RV_{cr}) for galloping. After finding the critical reduced velocity as a function of Scruton number, $RV_{cr} = f(Sc)$, for a fixed yaw angle, it was fitted with the curve whose form is given in Eq. (8), and the constants (a–c) in this equation are found. The results showing these constants of Eq. (8) for various yaw angles are summarized in Table 3. To validate RV_{cr} as a function of Sc given by Eq. (8) and Table 3, the plot corresponding to the critical yaw angle of 45° was compared with those from previous studies [20,25] (see Fig. 18), revealing good agreement with Saito's and Irwin's instability lines. Thus, these significant empirical equations (Table 3) can be used to predict the critical wind speed for dry-cable galloping of cables with different yaw/inclination angles. As explained before, galloping can be classified into unsteady galloping and classical galloping. The first type that is identified in wind-excited dynamic systems has an unsteady response with nonstationary amplitude. The second type that is a divergent-type galloping can be described by classical quasi-steady theory (Den-Hartog). This type of galloping normally occurs beyond the critical Reynolds number range of the cable where the lift coefficient is not zero and it occurs at a higher critical reduced velocity than the one corresponding to divergent-type galloping. In this study, free vibration test was used to determine the aerodynamic damping in a range of wind speeds below the critical wind speed of classical galloping where the unsteady galloping usually occurs. The physical free-vibration system

Table 3
Constants of Eq. (8) to predict reduced velocity.

$\beta°$	a	b	c
45°	7.03	0.6	46.07
40°	4.42	0.78	72.32
35°	5.95	0.79	86.33
30°	2.17	0.79	78.21
25°	3.32	0.78	70.71
20°	4.41	0.78	78.51
15°	1.23	0.8	81.94

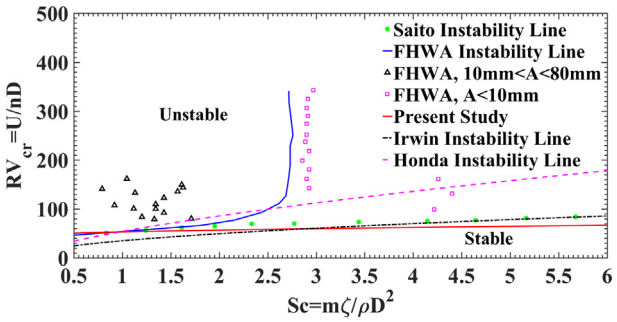

Fig. 18. Comparison of present result with other criteria for unstable and stable regions of dry-cable galloping.

used here did not allow testing the model at or beyond the critical wind speed. However, the aerodynamic damping curves of H_1^*, as obtained from the free vibration tests of the yawed cables, were extrapolated to predict the critical reduced velocity of classical galloping by using $H_1^* = 4Sc$ criterion when the total damping in the system goes to zero and divergent response occurs. Thus, the predicted critical reduced velocity based on our data corresponds to classical galloping and not unsteady galloping. Fig. 19 displays the critical reduced velocity vs Scruton number for various yaw angles 15°, 20°, 25°, 30°, 35°, 40°, and 45°.

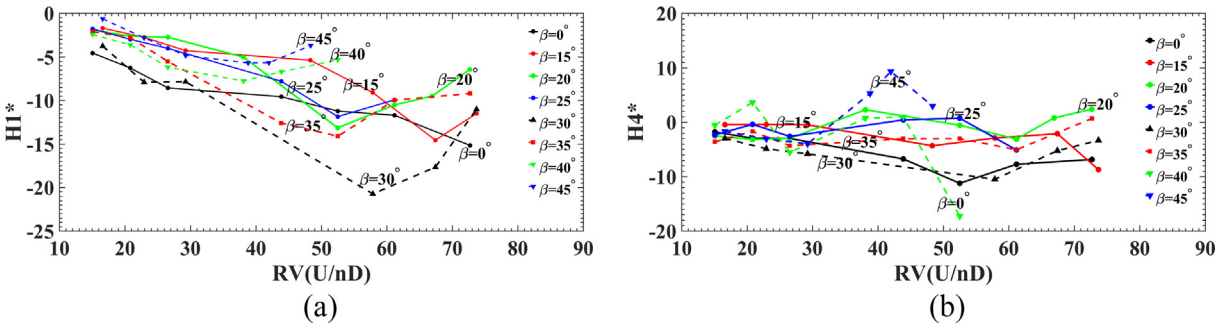

Fig. 16. Vertical flutter derivatives (1DOF) of yawed cable for different yaw angles, (a)H_1^*, (b)H_4^*.

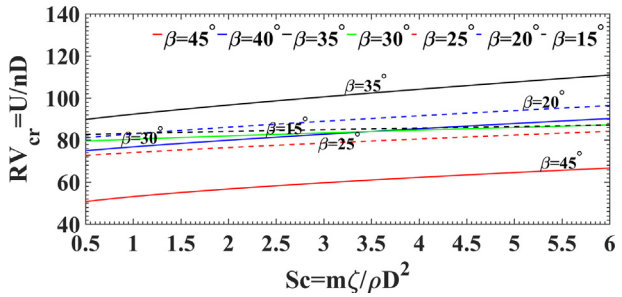

Fig. 19. Critical reduced velocity for dry-cable galloping vs. Scruton number for different yaw angles.

$$RV_{cr} = a * Sc^{b} + c \quad 0^{\circ} \leqslant \beta = \beta^{*} \leqslant 45^{\circ} \tag{8}$$

where constants a, b, and c are listed in Table 3.

Following a similar procedure, the flutter derivatives (P_1^*, P_4^*) for lateral motion (p) of the cable at a critical yaw angle of 45° were extracted for different reduced velocities (see Fig. 20). Fig. 21 shows a comparison of measured and simulated displacements (p) for $\beta = 45°$ case at a velocity of 5.9 m/s, revealing a good match between them. The P_1^* in Fig. 20a shows that it becomes increasingly negative with increasing RV which implies that the aerodynamic damping will become increasingly positive in the along-wind direction with increasing wind speed, ruling out any possibility of damping driven galloping or flutter in this lateral mode of vibration. Thus, the participation of the along-wind motion, which is generally true for cables that vibrate along inclined planes with elliptical trajectories, will add stability to the cable motion and thereby increase the critical reduced velocity for dry-cable galloping as predicted purely by vertical motion only (Eq. (8)).

5. Predicting minimum damping required

Finding the minimum additional damping required to stabilize the cables has always been a challenge for designing cables vulnerable to dry-cable galloping. Therefore, a simple and practical design procedure is introduced here in this section based on the obtained experimental data to estimate the required damping, which keeps cables stable. For any stay-cable in a cable-stayed bridge with a fixed inclination angle (α), for example, extreme wind is probable to come from a fixed direction at the given site where the bridge is located, yielding yaw angleβ for a plane of cables or individual cables as shown in Fig. 22. The procedure that is described here to calculate the additional damping required to mitigate dry-cable galloping in individual cables with relatively smooth surfaces can be applied to cables in other structures such as suspension bridges, suspended roofs, and low-voltage power transmission lines.

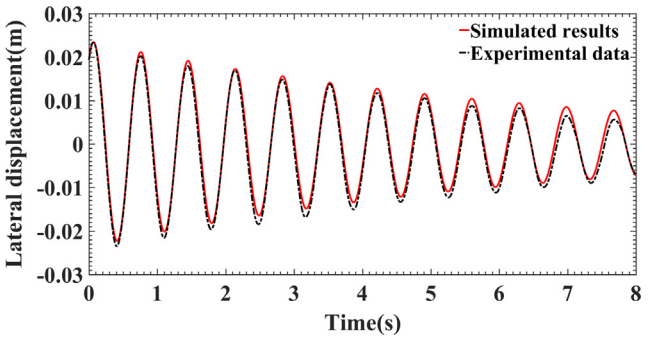

Fig. 21. Comparison of lateral displacement time history for $\beta = 45°$ at velocity of 5.9 m/s.

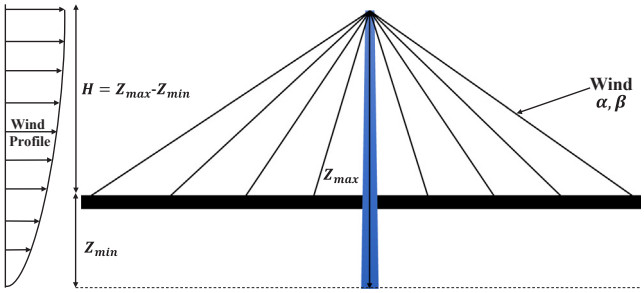

Fig. 22. Schematic view of inclined cables in cable-stayed bridge structure subject to ABL wind at a given yaw angle (β).

5.1. Design procedure

Design procedure of finding the required minimum damping is summarized in the following three steps.

Step 1

The equivalent yaw angle(β^*) can be calculated by Eq. (3) using the actual yaw angle (β) and inclination angle (α) of the cable.

Step 2

Since the profile of wind speed is a function of height and terrain type, these two parameters need to be specified. Mean wind speed profile can be estimated by the power law relationship as shown in Eq. (9). Using this equation, the mean hourly wind speed at any elevation z from the ground can be calculated based on the mean hourly wind speed at a height of 10 m (33 ft). In Eq. (9), α is the power-law exponent that depends on the terrain type.

$$\frac{U^{MH}(z)}{U^{MH}_{design}(10)} = \left(\frac{z}{10}\right)^{\alpha} \tag{9}$$

Since wind tunnel measurements are based on the mean hourly wind speed, all calculations should be based on mean hourly wind speed for cables in the field. Furthermore, since the wind speed is changing with

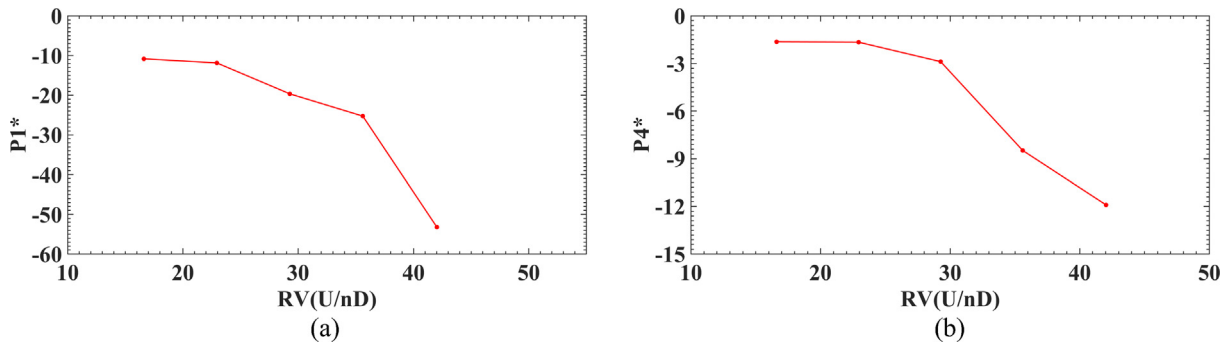

Fig. 20. Lateral flutter derivatives (1DOF) of yawed cable at $\beta = 45°$, (a) P_1^*, (b) P_4^*.

increasing height (z) over the height of an inclined cable, the average wind speed should be calculated. The average mean hourly (MH) design wind speed ($U^{MH}_{design} = \bar{U}_{design}$) can be estimated by Eq. (10). This equation is based on the 3-sec design speed, $U^{3-sec}_{design}(10)$,for the terrain over which the wind approaches the cable that can be estimated from $U^{3-sec,OT}_{design}(10)$, specified in ASCE 7-16 [39], as 3-sec gust in open terrain (OT) at 10 m (33 ft) height for various MRIs (mean recurrence intervals) at a given location where the cable is located using Eq. (11).

$$\bar{U}_{design} = \bar{U}^{MH}_{design} = \frac{\int_{Z_{min}}^{Z_{max}} U^{MH}_{design}(10)\left(\frac{z}{10}\right)^{\alpha} dz}{H} = \frac{U^{3-sec}_{design}(10)\int_{Z_{min}}^{Z_{max}}\left(\frac{z}{10}\right)^{\alpha} dz}{\lambda . H} \tag{10}$$

where $H = Z_{max} - Z_{min}$, Z_{min} and Z_{max} are the minimum and maximum elevation, respectively, of the inclined cable (Fig. 22) or suspended cable with a sag, and λ can be defined by Eq. (12), which relates the mean hourly wind speed and 3-sec gust speed at a height of 10 m for a particular terrain.

$$\frac{U^{3-sec}_{design}(10)}{U^{3-sec,OT}_{design}(10)} = \frac{u_*}{u_*^{OT}} \frac{\ln\frac{10}{z_0}}{ln\frac{10}{0.07}} \tag{11}$$

where u_* and u_*^{OT} are friction velocity for the given terrain of the approaching flow and open terrain, respectively, z_0 is roughness length in meters of the terrain of the approaching flow. $\frac{u_*}{u_*^{OT}}$ can be estimated from Table 4 [40].

$$\frac{U^{3-sec}_{design}(10)}{U^{MH}_{design}(10)} = \left(1 + \frac{\sqrt{\gamma}\, c(3)}{2.5\ln\left(\frac{10}{z_0}\right)}\right) = \lambda \tag{12}$$

where$c(3) = 2.85$, z_0 is roughness length in meters of the terrain of the approaching flow, γ is a constant that depends on the roughness length, as shown in Table 4 [40]. Thus, the average of mean hourly design wind speed ($\bar{U}_{design}$)can be estimated based on above-mentioned equations (Eqs. (10)–(12)) by defining terrain type and configuration of the cables.

Step 3

The relationship between critical reduced velocity and Scruton number, $RV_{cr} = fn(Sc)$, that is defined in Eq. (8), and Table 3 for different yaw angles β is used where β in these empirical equations is the same as the equivalent yaw angle β^* estimated for the cable. Since it is theoretically proven that dimensionless numbers are equivalent, $RV_{design} = \frac{\bar{U}_{design}}{fD} = RV_{cr} = fn(Sc)$, it can be shown that design reduced velocity is a function of a design Scruton number (Sc^{design}). Thus, the desired or design Scruton number (Sc^{design}) for a cable with natural frequency (f) and cable diameter (D) should be calculated to estimate the required damping in a cable to avoid dry-cable galloping in a given dynamic mode up to the design wind speed. The design Scruton number to prevent dry-cable galloping can be extracted (see Fig. 23) by knowing average design wind speed, equivalent yaw angle, cable diameter, and cable natural frequencies. For different equivalent yaw angles, the relationship between Scruton number (log scale) and average design wind speed (mean hourly) is shown in Fig. 23 for a constant parameter of fD varying in the range of 0.1–1.1. It is worth mentioning that the range of average design wind speed ($\bar{U}_{design}$) and fD were selected to cover most of the cables vibrating in the first three dynamic modes. Subsequently, the minimum required damping (ζ^m) can be predicted by finding the design Scruton number ($Sc^{design} = (\frac{m_e \zeta^m}{\rho D^2})$) from Fig. 23, where m_e is generalized mass per unit length of the cable based on the dynamic mode of excitation considered, ζ^m is minimum damping required, ρ is air density, and D is cable diameter. Fig. 24 illustrates the flow chart, which summarizes the mentioned design procedure to predict the required damping. Additional damping that is required to prevent large amplitude vibration due to dry-cable galloping can be provided through either mechanical damper or aerodynamic damper or a combination thereof. It can be estimated by subtracting the inherent mechanical damping in the cable from the required damping.

Table 4
Variable γ corresponding to various roughness lengths [40].

Z_0 (m)	0.005	0.07	0.30	1.00	2.50
γ	6.50	6.00	5.25	4.85	4.00
$\frac{u_*}{u_*^{OT}}$	0.83	1.00	1.15	1.33	1.46

6. Conclusions

Inclined cables of long-span bridges have frequently experienced moderate to large-amplitude motions during the past few decades because of phenomena such as rain-wind induced vibration, vortex-induced vibration, iced-cable galloping, wake galloping, and dry-cable galloping. In this paper, dry-cable galloping was studied by conducting wind tunnel tests to measure the aerodynamic and aeroelastic loads of a yawed dry cable. A series of static and dynamic experiments were performed to extract flutter derivatives and buffeting indicial derivative functions associated with self-excited and buffeting loads, respectively. For this purpose, all experiments were conducted on a section model of a smooth cable under uniform and smooth/gusty flow conditions in the AABL Wind and Gust Tunnel. According to the literature, the aerodynamic behavior of an inclined and/or yawed cable can be found from that of a yawed cable only using the definition of equivalent yaw angle. For the sake of simplicity, all wind tunnel experiments were conducted only for a yawed cable, and the results can be applied to find the aerodynamic properties of an inclined and/or yawed cable. Static wind tunnel tests of surface pressure distribution and load measurements on a cable model resulted in proposing an empirical equation for predicting the mean drag coefficient and Strouhal number for yaw angles ranging from 0° to 45° while the mean lift coefficient was found to be zero in the subcritical Reynolds number regime. Results indicate that the mean drag coefficient decreases with increasing yaw angles, which would increase the vulnerability of the dry-cable galloping following the Den-Hartog criterion. For buffeting tests, aerodynamic admittance functions and buffeting indicial derivative functions for the yawed cables were extracted for various yaw angles in the range of 0–45° and empirical equations were proposed for the same, which would be useful for computing buffeting loads at various yaw angles. The results show that the aerodynamic admittance function at a given reduced velocity has a lower value in the along-wind direction (χ_p^2) and has a higher value in the across-wind direction (χ_h^2) for cables at higher yaw angles. For dynamic 1DOF tests, vertical and lateral flutter derivatives (H_1^*, H_4^*, P_1^*, P_4^*) of a yawed cable were identified from a measured response of a section model in free vibration for yaw angles ranging from 0° to 45°. Empirical equations were extracted to predict the critical wind speed for dry-cable galloping of a cable at a specific yaw angle based on its Scruton number. Results showed that the critical equivalent yaw angle is 45° for dry-cable galloping in vertical motion. Additionally, a strong agreement between the present instability criterion for dry-cable galloping based on the critical equivalent yaw angle and those from two other well-known studies was found. In the present study, separate instability criterion was found for cables with different equivalent yaw angles. Finally, a simplified design procedure was introduced to estimate the minimum damping required to prevent the dry-cable galloping up to the design wind speed of the cable structure, which will help to estimate the additional damping required for an individual cable based on its orientation and site characteristics of the cable structure's location. Furthermore, the aerodynamic and aeroelastic cable load parameters obtained here are significantly helpful in predicting the response of inclined/yawed cables at a specific wind speed and in predicting the critical wind speed for dry-cable galloping.

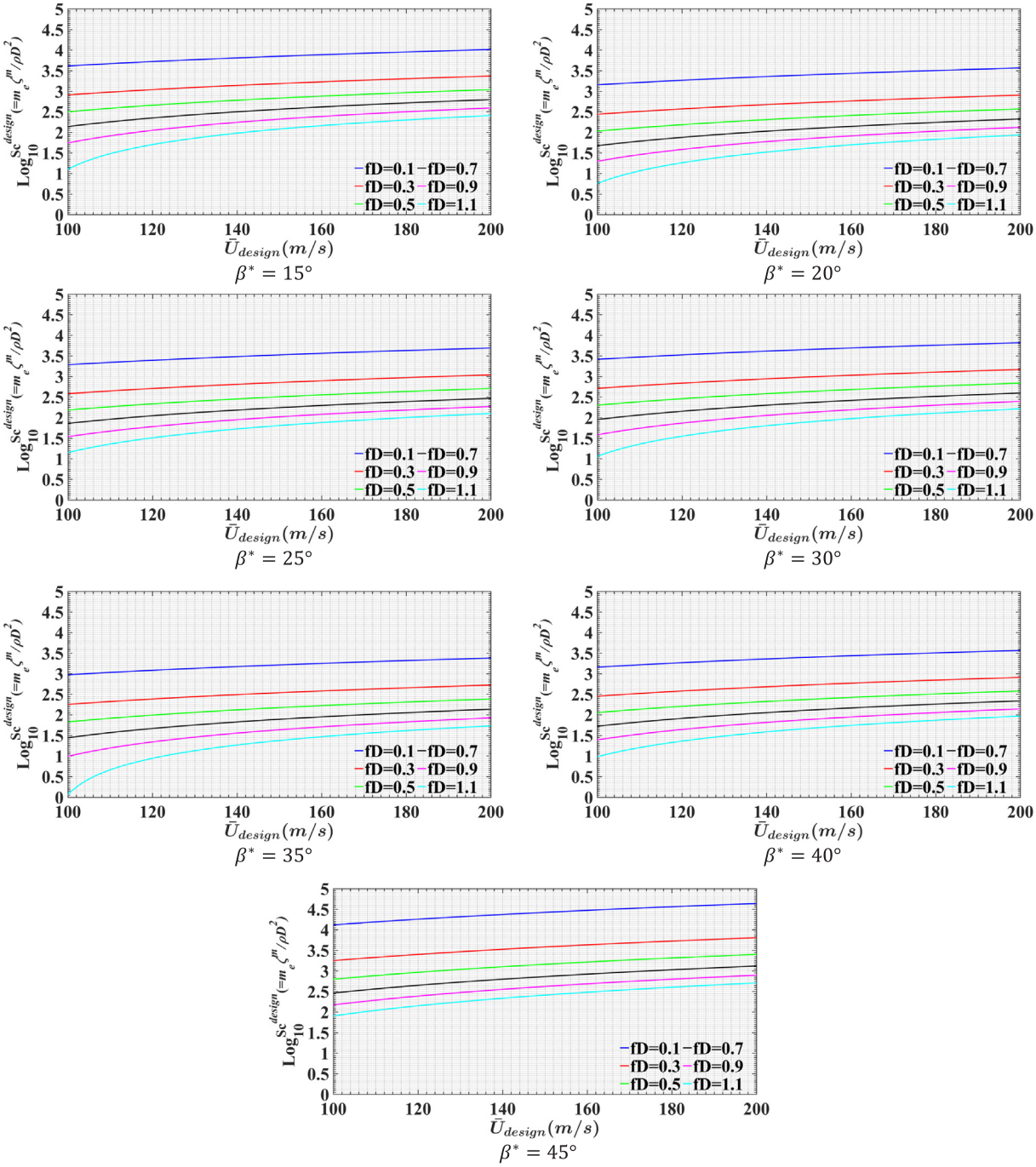

Fig. 23. Design Scruton number (Sc^{design}) vs. average design wind speed (mean hourly, $\bar{U}_{design}$) for cables with different cable parameter (fD) and equivalent yaw angle (β^*).

Acknowledgement

The authors gratefully acknowledge the U.S. National Science Foundation (NSF) for the financial support of this study under research grant CMMI-1537917.

Appendix A. Self-excited force

Self-excited loads are motion-induced loads that are proportional to displacements and velocities of the cable motion and mean speed of the incoming wind. Parameters describing these loads can be extracted using two methods: direct measurement of aerodynamic force using strain gauges, or indirect measurement using a free vibration or forced vibration wind tunnel test [41]. The following equation describes the extraction of H_1^* and H_4^* for 1 degree of freedom (DOF) tests. The general equation of motion for a structure due to self-excited loads of vertical motion is defined as follows:

$$\ddot{h} + M^{-1}C\dot{h} + M^{-1}kh = M^{-1}F_{se} \tag{A.1}$$

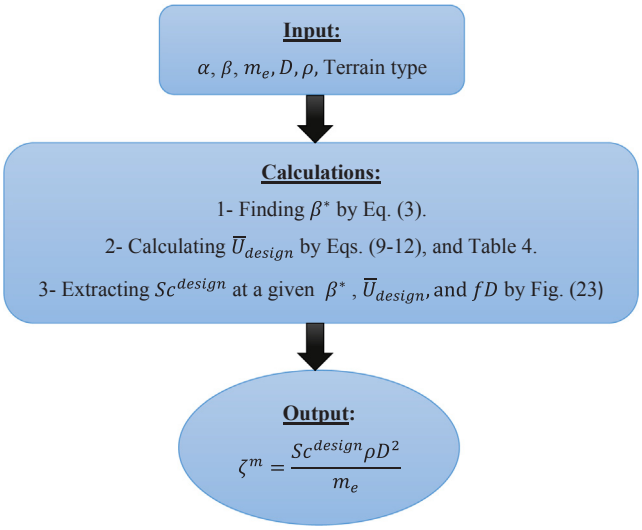

Fig. 24. Flow chart of estimating the minimum damping (ζ^m) required to prevent dry-cable galloping.

where $M = m_h$, $M^{-1}C = 2\zeta_h\omega_h$, $M^{-1}k = \omega_h^2$

and the aeroelastic force (F_{se}) is given in Eq. (A.2).

$$F_{se} = 0.5\rho U^2 D\,[KH_1^*/UK^2H_4^*/D]\begin{bmatrix}\dot{h}\\ h\end{bmatrix} \tag{A.2}$$

where K is reduced frequency ($K = \omega D/U$), ω is angular frequency, D is a typical across-wind dimension of the cross-section of the structure or cable diameter here, and U is mean wind speed. By substituting Eq. (A.2) into Eq. (A.1) and gathering all terms to the left hand side, the modified free-vibration equation including aeroelastic effects is

$$\ddot{h} + C^{eff}\dot{h} + K^{eff}h = 0 \tag{A.3}$$

where C^{eff} and K^{eff} are the aeroelastically modified effective damping and stiffness, respectively. In addition, if C^{mech} and K^{mech} are mechanical damping and stiffness under zero-wind conditions, the flutter derivatives H_1^* and H_4^* can be derived as follows:

$$H_1^*(K) = -\frac{2m_h}{\rho D^2\omega}(C^{eff} - C^{mech}) \tag{A.4}$$

$$H_4^*(K) = -\frac{2m_h}{\rho D^2\omega^2}(K^{eff} - K^{mech}) \tag{A.5}$$

An iterative least-squares (ILS) method was used for the extraction of flutter derivatives. This system identification method was successfully used to extract 2 flutter derivatives associated with 1DOF, 8 flutter derivatives associated with 2DOF, and 18 flutter derivatives associated with 3DOF section model of a bridge [41]. To apply this method, the displacement response of a section model that is released from a fixed state of rest with an initial displacement, measured in free vibration, is filtered digitally and used as an input to this method. A MATLAB code was used in which a "Butterworth" filter was employed as a low-pass filter to remove all noises from the recorded displacement time history with frequencies higher than the natural frequency of the section model. In the ILS method, a state-space model is used as given by Eq. (A.6).

$$\dot{\underline{X}} = \underline{A}\cdot\underline{X} \tag{A.6}$$

where

$$\underline{X} = \begin{bmatrix}h\\ \dot{h}\end{bmatrix},\quad \underline{A} = \begin{bmatrix}0 & 1\\ -K^{eff} & -C^{eff}\end{bmatrix}$$

$\underline{A}$ is a 2×2 square matrix. After calculating the filtered displacement time history from the measured time history displacement and calculating the velocity, $\dot{h}$, and acceleration, $\ddot{h}$, time histories of the section model, $\underline{A}$ or C^{eff} and K^{eff} can be identified using the ILS method at a given wind speed and by subtracting their zero wind values C^{mech} and K^{mech}, respectively, H_1^* and H_4^* can be extracted at a given wind speed using Eqs. (A.4) and (A.5). Full description of the ILS method can be obtained in [41]. For maintaining accuracy, all initial displacements and sampling time of the time history records were kept the same for all wind speeds. Similarly, flutter derivatives for lateral motion (p), P_1^* and P_4^*, can be extracted by conducting free vibration tests along the lateral motion.

Appendix B. Buffeting load

This type of wind load that originates due to wind turbulence can be calculated in time domain for both vertical and lateral DOFs, as given by Eqs. (B.1) and (B.2).

$$F_b^h(s) = 0.5\rho UD \int_0^s [\, 2C_L u(\sigma)\phi_h^{'}(s-\sigma) + (C_D + C_L^{'})w(\sigma)\phi_h^{'}(s-\sigma)]d\sigma \tag{B.1}$$

$$F_b^p(s) = 0.5\rho UD \int_0^s [2C_D u(\sigma)\phi_p^{'}(s-\sigma) - C_L w(\sigma)\phi_p^{'}(s-\sigma)]d\sigma \tag{B.2}$$

where ρ= air density, U = mean wind speed, C_D = drag coefficient, D = cable diameter, $C_L^{'} = \frac{dC_L}{d\alpha}$, $u(\sigma)$ and$w(\sigma)$ = zero mean wind turbulence components in along and across-wind directions, respectively, $s = Ut/D$ = non-dimensional time, $\phi_h^{'}(s)$ and $\phi_p^{'}(s)$ are derivatives of buffeting indicial functions $\phi_h(s)$ and $\phi_p(s)$ with respect to 's', respectively, referred here as buffeting indicial derivative functions that can be extracted using the aerodynamic admittance functions $\chi_h^2(K)$ and $\chi_p^2(K)$ (Eqs. (B.3)–(B.4)). Aerodynamic admittance functions, $\chi_h^2(K)$ and $\chi_p^2(K)$, are functions of reduced frequency (K) that relate turbulence in upstream wind flow to the fluctuating wind load in the frequency domain [42]. To extract the aerodynamic admittance functions of a cable in the frequency domain, Eqs. (B.3) and (B.4) can be used.

$$S_{F_b^h F_b^h}(K) = \left(\tfrac{1}{2}\rho U^2 D\right)^2 \left[(2C_L)^2 \tfrac{S_{uu}(K)}{U^2} + (C_D + C_L^{'})^2 \tfrac{S_{ww}(K)}{U^2} \right] \chi_h^2(K) \tag{B.3}$$

$$S_{F_b^p F_b^p}(K) = \left(\frac{1}{2}\rho U^2 D\right)^2 \left[4C_D^2 \frac{S_{uu}(K)}{U^2} + C_L^{'2} \frac{S_{ww}(K)}{U^2} \right] \chi_p^2(K) \tag{B.4}$$

where $S_{F_b^h F_b^h}(K)$ and $S_{F_b^p F_b^p}(K)$ are power spectral densities of the buffeting load in across- and along-wind directions, respectively, $S_{uu}(K)$ and $S_{ww}(K)$ are power spectral densities of wind turbulence in along- and across-wind directions, respectively, and $\chi_h^2(K)$ and $\chi_p^2(K)$ are aerodynamic admittance functions in vertical and lateral directions. The buffeting indicial derivative function takes the form given in Eq. (B.5). In this study, only two terms are used to model the buffeting indicial derivative functions (Eq. (B.5)) because a past study [42] has demonstrated that two terms are enough to accurately model these functions and the addition of the third term does not improve the accuracy of the predicted buffeting loads using these functions.

$$\phi^{'}(s) = A_1 e^{-A_2 s} + A_3 e^{-A_4 s} \tag{B.5}$$

where $A_i, i = 1.4$, are constants that can be computed for each of the two DOFs using Eq. (B.6) that is derived from the Fourier transform relationship between the aerodynamic admittance function, as identified from wind tunnel tests, and buffeting indicial derivative function.

$$\chi^2(K) = \left(\frac{A_1 \cdot K}{A_2^2 + K^2} + \frac{A_3 \cdot K}{A_4^2 + K^2} \right)^2 + \left(\frac{A_1 \cdot A_2}{A_2^2 + K^2} + \frac{A_3 \cdot A_4}{A_4^2 + K^2} \right)^2 \tag{B.6}$$

Finally, buffeting loads in time domain can be computed for both vertical and lateral DOFs by applying Eqs. (B.1) and (B.2) after identifying the buffeting indicial derivative functions.

References

[1] Cheng P, Li WJ, Chen WL, Gao DL, Xu Y, Li H. Computer vision-based recognition of rainwater rivulet morphology evolution during rain–wind-induced vibration of a 3D aeroelastic stay cable. J Wind Eng Ind Aerodyn 2018;172:367–78.
[2] Jing H, Xia Y, Li H, Xu Y, Li Y. Excitation mechanism of rain–wind induced cable vibration in a wind tunnel. J Fluids Struct 2017;68:32–47.
[3] Ge Y, Chang Y, Xu L, Zhao L. Experimental investigation on spatial attitudes, dynamic characteristics and environmental conditions of rain–wind-induced vibration of stay cables with high-precision raining simulator. J Fluids Struct 2018;76:60–83.
[4] Chen WL, Zhang QQ, Li H, Hu H. An experimental investigation on vortex induced vibration of a flexible inclined cable under a shear flow. J Fluids Struct 2015;54:297–311.
[5] Wang J, Fu S, Baarholm R, Wu J, Larsen CM. Fatigue damage induced by vortex-induced vibrations in oscillatory flow. Marine Struct 2015;40:73–91.
[6] Park J, Kim S, Kim HK. Effect of gap distance on vortex-induced vibration in two parallel cable-stayed bridges. J Wind Eng Ind Aerodyn 2017;162:35–44.
[7] Foti F, Martinelli L. Finite element modeling of cable galloping vibrations. Part II: Application to an iced cable in 1: 2 multiple internal resonance. J Vib Control 2018;24(7):1322–40.
[8] Yan Z, Li Z, Savory E, Lin WE. Galloping of a single iced conductor based on curved-beam theory. J Wind Eng Ind Aerodyn 2013;123:77–87.
[9] Gurung CB, Yamaguchi H, Yukino T. Identification of large amplitude wind-induced vibration of ice-accreted transmission lines based on field observed data. Eng Struct 2002;24(2):179–88.
[10] Tokoro S, Komatsu H, Nakasu M, Mizuguchi K, Kasuga A. A study on wake-galloping employing full aeroelastic twin cable model. J Wind Eng Ind Aerodyn 2000;88(2–3):247–61.
[11] He X, Cai C, Wang Z, Jing H, Qin C. Experimental verification of the effectiveness of elastic cross-ties in suppressing wake-induced vibrations of staggered stay cables. Eng Struct 2018;167:151–65.
[12] Tanaka T, Matsumoto M, Ishizaki H, Kibe H. Dry galloping characteristic and vibration control of inclined stay cable. In: Proceedings of the 1st international symposium on flutter and its application; 2017. p. 639.
[13] Demartino C, Ricciardelli F. Assessment of the structural damping required to prevent galloping of dry HDPE stay cables using the quasi-steady approach. J Bridge Eng 2018;23(4):04018004.
[14] Vo DH, Katsuchi H, Yamada H. Dry galloping of surface modification cable in low Scruton number range. In: Proceedings of the 1st international symposium on flutter and its application; 2017. p. 629–38.
[15] Piccardo G, Zulli D, Luongo A. Dry galloping in inclined cables: linear stability analysis. Procedia Eng 2017;199:3164–9.
[16] Benidir A, Flamand O, Dimitriadis G. The impact of circularity defects on bridge stay cable dry galloping stability. J Wind Eng Ind Aerodyn 2018;181:14–26.
[17] Matsumoto M. Effects of axial flow and Karman vortex interference on dry-state galloping of inclined stay-cables. In: Proceedings of the 6th international symposium on cable dynamics; 2005.
[18] Honda A, Yamanaka T, Fujiwara T, Saito T. Wind tunnel test on rain-induced vibration of the stay-cable. In: Proceedings of the international symposium on cable dynamics; 1995. p. 255–62.
[19] Irwin P. Wind vibrations of cables on cable-stayed bridges. Struct Cong 1997:383–7.
[20] Kumarasena S, Jones NP, Irwin P, Taylor P. Wind-induced vibration of stay cables. FHWA-HRT-05-083. U.S. Department of Transportation, Federal Highway Administration; 2007.
[21] Saito T, Matsumoto M, Kitazawa M. Rain-wind excitation of cables on cable-stayed Higashi-Kobe Bridge and cable vibration control. In: Proceedings of the international conference on cable-stayed and suspension bridges; 1994. p. 507–14.
[22] Cheng S, Larose GL, Savage MG, Tanaka H, Irwin PA. Experimental study on the wind-induced vibration of a dry inclined cable—Part I: Phenomena. J Wind Eng Ind Aerodyn 2008;96(12):2231–53.
[23] Cheng S, Irwin PA, Tanaka H. Experimental study on the wind-induced vibration of a dry inclined cable—Part II: Proposed mechanisms. J Wind Eng Ind Aerodyn 2008;96(12):2254–72.
[24] Duy HV, Katsuchi H, Yamada H, Nishio M. Experimental study on dry-state galloping with various wind relative angles and its countermeasures. J Struct Eng 2014;60A:428–36.
[25] Matsumoto M, Yagi T, Hatsuda H, Shima T, Tanaka M, Naito H. Dry galloping characteristics and its mechanism of inclined/yawed cables. J Wind Eng Ind Aerodyn 2010;98(6–7):317–27.
[26] Katsuchi H, Yamada H. Wind-tunnel study on dry-galloping of indented-surface stay cable. In: Proceedings of the 11th Americas conference on wind engineering; 2009, p. 22–6.
[27] Benidir A, Flamand O, Gaillet L, Dimitriadis G. Impact of roughness and circularity-defect on bridge cables stability. J Wind Eng Ind Aerodyn 2015;137:1–3.
[28] Flamand O, Boujard O. A comparison between dry cylinder galloping and rain-wind induced excitation. In: Proceedings of the 5th European & African conference on wind engineering (EACWE5); 2009. p. 5.
[29] Kleissl K, Georgakis CT. Aerodynamic control of bridge cables through shape modification: a preliminary study. J Fluids Struct 2011;27(7):1006–20.

[30] Ma WY, Liu QK, Du XQ, Wei YY. Effect of the Reynolds number on the aerodynamic forces and galloping instability of a cylinder with semi-elliptical cross sections. J Wind Eng Ind Aerodyn 2015;146:71–80.
[31] Nikitas N, Macdonald JH. Aerodynamic forcing characteristics of dry cable galloping at critical Reynolds numbers. Eur J Mech B Fluids 2015;49:243–9.
[32] Macdonald JH, Larose GL. A unified approach to aerodynamic damping and drag/lift instabilities, and its application to dry inclined cable galloping. J Fluids Struct 2006;22(2):229–52.
[33] Raeesi A, Cheng S, Ting DS. Aerodynamic damping of an inclined circular cylinder in unsteady flow and its application to the prediction of dry inclined cable galloping. J Wind Eng Ind Aerodyn 2013;113:12–28.
[34] Wu X, Sharma A, Jafari M, Sarkar P. Towards predicting dry cable galloping using detached eddy simulations. In: 55th AIAA Aerospace Sciences Meeting; 2017, p. 1483.
[35] Yeo D, Jones NP. A mechanism for large amplitude, wind-induced vibrations of stay cables. In: Proceedings of the 11th Americas Conference on Wind Engineering, San Juan; 2009.
[36] Luongo A, Zulli D, Piccardo G. On the effect of twist angle on nonlinear galloping of suspended cables. Comput Struct 2009;87(15–16):1003–14.
[37] Phelan RS, Sarkar PP, Mehta KC. Full-scale measurements to investigate rain–wind induced cable-stay vibration and its mitigation. J Bridge Eng 2006;11(3):293–304.
[38] Chiu WS, Lienhard JH. On real fluid flow over yawed circular cylinders. J Basic Eng 1967;89(4):851–7.
[39] ASCE/SEI 7-16. Minimum design loads and associated criteria for buildings and other structures. American Society of Civil Engineers (ASCE)/Structural Engineering Institute (SEI); 2017.
[40] Simiu E, Scanlan RH. Wind effects on structures: fundamentals and applications to design. 3rd ed. New York (USA): John Wiley and Sons; 1996.
[41] Chowdhury AG, Sarkar PP. A new technique for identification of eighteen flutter derivatives using a three-degree-of-freedom section model. Eng Struct 2003;25(14):1763–72.
[42] Chang B, Sarkar P, Phares B. Time-domain model for predicting aerodynamic loads on a slender support structure for fatigue design. J Eng Mech 2009;136(6):736–46.